Open access • Journal Article • DOI:10.2118/155640-PA

Gas Flow Tightly Coupled to Elastoplastic Geomechanics for Tight- and Shale-Gas Reservoirs: Material Failure and Enhanced Permeability — Source link

Ji-Hoon Kim, George J. Moridis

Institutions: Lawrence Berkeley National Laboratory

Published on: 01 Dec 2014 - Spe Journal (Society of Petroleum Engineers (SPE))

Topics: Tight gas, Permeability (earth sciences), Geomechanics and Shear stress

Title

Gas Flow Tightly Coupled to Elastoplastic Geomechanics for Tight- andShale-Gas Reservoirs: Material Failure and Enhanced Permeability

Authors

Kim, Jihoon
Moridis, George

Publication Date

2014-12-01

Gas Flow Tightly Coupled to Elastoplastic Geomechanics for Tight- and Shale-Gas Reservoirs: Material Failure and Enhanced Permeability

Jihoon Kim and George J. Moridis, Lawrence Berkeley National Laboratory

This report has been published in *SPE Journal*, **19** (6) 1110-1125 (December 2014) and is viewable on line at : http://dx.doi.org/10.2118/155640-PA

.

Abstract

We investigate coupled flow and geomechanics in gas production from extremely low permeability reservoirs such as tight and shale gas reservoirs, using dynamic porosity and permeability during numerical simulation. In particular, we take the intrinsic permeability as a step function of the status of material failure, and the permeability is updated every time step. We consider gas reservoirs with the vertical and horizontal primary fractures, employing the single and dynamic double porosity (dual continuum) models. We modify the multiple porosity constitutive relations for modeling the double porous continua for flow and geomechanics. The numerical results indicate that production of gas causes redistribution of the effective stress fields, increasing the effective shear stress and resulting in plasticity. Shear failure occurs not only near the fracture tips but also away from the primary fractures, which indicates generation of secondary fractures. These secondary fractures increase the permeability significantly, and change the flow pattern, which in turn causes a change in distribution of geomechanical variables. From various numerical tests, we find that shear failure is enhanced by a large pressure drop at the production well, high Biot's coefficient, low frictional and dilation angles. Smaller spacing between the horizontal wells also contributes to faster secondary fracturing. When the dynamic double porosity model is used, we observe a faster evolution of the enhanced permeability areas than that obtained from the single porosity model, mainly due to a higher permeability of the fractures in the double porosity model. These complicated physics for stress sensitive reservoirs cannot properly be captured by the uncoupled or flow-only simulation, and thus tightly coupled flow and geomechanical models are highly recommended to accurately describe the reservoir behavior during gas production in tight and shale gas reservoirs and to smartly design production scenarios.

Introduction

Unconventional natural gas such as tight and shale gas has become an increasingly important source of natural gas in the United States over the past decade and the estimates of the natural gas resource potential for shale gas range from 14.16×10^{12} m^3 to 28.3×10^{12} m^3 (500~1000 Tcf) (Arthur et al. 2008; Jenkins and Boyer 2008). Geological formations of tight and shale gas reservoirs exhibit extremely low permeability within which gas is trapped (Hill and Nelson 2000), and accordingly hydraulic fracturing is performed in order to enhance permeability and increase production rate (Dean and Schmidt 2008; Ji et al. 2009; Nassir et al. 2012). The success of gas production from the Barnett Shale is based on horizontal wells and hydraulic fracturing techniques and has led to gas production of other shale reservoirs such as the Marcellus Shale, one of the largest natural gas resources in the United States (Arthur et al. 2008; Cipolla et al. 2010).

Several studies have been made on production of gas from tight and shale gas reservoirs as well as hydraulic fracturing. Freeman et al. (2011) investigated non-Darcy flow without geomechanics, examining the effects of Knudsen diffusion on gas composition, because flow mechanism of shale gas is significantly different from that of conventional oil and gas reservoirs due to extremely low permeability and small pore throat. Vermylen and Zoback (2011) studied different scenarios for hydraulic fracturing along horizontal wells, and found significant differences in stimulation robustness for different fracturing procedures, for example, between alternatively fractured (zipperfrac) and simultaneously fractured (simulfrac) wells. Ji et al. (2009) developed a numerical model for hydraulic fracturing, accounting for coupled flow and geomechanics, and Nassir et al. (2012) partially incorporated shear failure within a primary fracture obtained from tensile fracturing. Dean and Schmidt (2008) employed the same fracturing idea as Ji et al. (2009), using different criteria of fracture propagation. Fisher and Warpinski (2012) analyzed the fracture growth induced by hydraulic fracturing with real data, and concluded that the fracture propagation was limited in the vertical direction, compared with the horizontal direction. Yet, coupled flow and geomechanics that can consider dynamic interrelations among pore volume, permeability, and material failure during production are little investigated. Geomechanics with material failure may change permeability and porosity followed by flow patterns significantly, and, in turn, redistribution of pore-pressure can affect geomechanics (e.g., Armero (1999) and Rutqvist and Stephansson (2003)). Thus, rigorous modeling for coupled flow and geomechanics is necessary for gas production in shale and tight gas reservoirs.

In this study, we perform numerical simulations of coupled flow and geomechanics in shale and tight gas reservoirs, focusing on geological failure and secondary fracturing of intact rock, which can increase permeability. To this end, we consider variations in not only permeability but also pore volume, which lead to dynamic permeability and porosity of the reservoirs, respectively. In particular, compaction in undrained condition such as low permeability induces the increase of pore-pressure, which can change effective stress fields significantly and may result in geological failure (Kim et al., 2012a). Compaction-induced shear failure by fluid production was also studied by Dusseault et al. (2001) and Bagheri and Settari (2008).

For secondary fracturing, we employ the Mohr-Coulomb failure model for elastoplasticity, which is widely used to model failure in cohesive frictional materials, shear failure. We also use dynamic permeability, which is a function of the failure status. Single-porosity and (dynamic) double-porosity models are both investigated. One may introduce double porosity and permeability in flow for better accurate modeling of flow because fractures occupy a much smaller fraction of bulk volume of a gridblock than rock matrix (Barenblatt et al.1960; Pruess and Narasimhan 1985; Bagheri and Settari 2008). On the other hand, it is required to use a slightly different geomechanics, because return mapping for elastoplasticity that models rock failure is performed at the gridblock level, not subelements of the gridblock. Note that the geomechanics still accounts for both geomechanical moduli of the fracture and intact rock. Then, in the case of the double porosity model in flow and geomechanics, we modify the constitutive relations proposed by Kim et al. (2012b), which generalized the constitutive model by Berryman (2002) to non-isothermal multiple porosity coupled flow and geomechanics systems.

For numerical simulation, we use a sequential implicit method, employing the fixed-stress split, which can provide unconditional stability and high accuracy, considering two-way coupling between flow and geomechanics (Settari and Mourits 1998; Kim et al. 2011a, b). Specifically, flow is solved first, fixing the total stress fields and calculating the contribution of geomechanics to flow explicitly, and then geomechanics is solved from the solutions obtained at the previous flow step. We employ finite volume and finite element methods for flow and geomechanics in space discretization, respectively, and the backward Euler method in time discretization.

We will perform numerical simulations for given horizontal and vertical primary single fractures, under horizontal well production scenarios. From the simulation, we will find that shear failure occurs not only near the tips of the primary fractures but also away from the fractures during production, generating secondary fractures, because production of gas causes redistribution of the effective stress fields over the domain instantaneously, increasing the effective shear stress and resulting in failure. From numerical tests, we will also find that shear failure is enhanced by a low bottom hole pressure, high Biot's coefficient, low frictional and dilation angles, and small spacing between the horizontal wells. Secondary fractures increase permeability dramatically, which is a welcome development as it enhances gas production. The risk of potential detrimental environmental effects (e.g., through creation of a conduit to overlying aquifers) appears low because of the limited extent of the secondary fractures, but a definitive answer will require more focused study of this problem. This physics cannot be captured accurately by uncoupled or flow-only simulation, and thus tightly coupled flow and geomechanics are highly recommended for gas production in shale gas reservoirs.

Mathematical formulation

We describe the governing equations for fluid and heat flow, as explained in Pruess et al. (1999). The governing equation for multiphase and multi-component flow comes from mass balance as

$$\frac{d}{dt}\int_{\Omega} m^k d\Omega + \int_{\Gamma} \mathbf{f}^k \cdot \mathbf{n} d\Gamma = \int_{\Omega} q^k d\Omega \ , \tag{1}$$

where the superscript k indicates the fluid component. $d(\cdot)/dt$ means the time derivative of a physical quantity $(\cdot)$ relative to the motion of the solid skeleton. m^k is mass of component k. $\mathbf{f}^k$, and q^k are its flux and source terms on the domain Ω with the boundary Γ, respectively, where $\mathbf{n}$ is the normal vector of the boundary.

The mass of component k is written as

$$m^k = \sum_J \phi S_J \rho_J X_J^k \ , \tag{2}$$

where the subscript *J* indicates fluid phases. ϕ is the true porosity, defined as the ratio of the pore volume to the bulk volume in the *deformed* configuration. S_J, ρ_J, and X_J^k are saturation and density of phase *J*, and the mass fraction of component *k* in phase *J*, respectively.

The mass flux term is obtained from

$$\mathbf{f}^k = \sum_J (\mathbf{w}_J^k + \mathbf{J}_J^k) \ , \tag{3}$$

where $\mathbf{w}_J^k$ and $\mathbf{f}_J^k$ are the convective and diffusive mass flows of component *k* in phase *J*. For the liquid phase, *J*=*L*, $\mathbf{w}_L^k$ is given by Darcy's law as

$$\mathbf{w}_L^k = X_L^k \mathbf{w}_L \ , \ \mathbf{w}_L = -\frac{\rho_L k_{rL}}{\mu_L}\mathbf{k}\left(\mathbf{Grad}p_L - \rho_L \mathbf{g}\right) , \tag{4}$$

where **k** is the absolute (intrinsic) permeability tensor. μ_J, k_{rJ}, p_J are the viscosity, relative permeability, and pressure of the fluid phase *J*, respectively. $\mathbf{g}$ is the gravity vector, and $\mathbf{Grad}$ is the gradient operator. For the gaseous phase, *J*=*G*, $\mathbf{w}_G^k$ is given by

$$\mathbf{w}_G^k = X_G^k \mathbf{w}_G \ , \ \mathbf{w}_G = -\left(1 + \frac{k_K}{p_G}\right)\frac{\rho_G k_{rG}}{\mu_G}\mathbf{k}\left(\mathbf{Grad}p_G - \rho_G \mathbf{g}\right) , \tag{5}$$

where k_K is the Klinkenberg factor.

The diffusive flow can be written as

$$J_J^k = -\phi S_J \tau_J \rho_J \mathbf{D}_J^k \mathbf{Grad} X_J^k \ , \tag{6}$$

where $\mathbf{D}_J^k$ and τ_J are the hydrodynamic dispersion tensor and tortuosity for phase *J* and component *k*.

The governing equation for heat flow comes from energy (heat) balance, as

$$\frac{d}{dt}\int_\Omega m^H d\Omega + \int_\Gamma \mathbf{f}^H \cdot \mathbf{n} d\Gamma = \int_\Omega q^H d\Omega \ , \tag{7}$$

where the superscript H indicates the heat component. m^H, $\mathbf{f}^H$, and q^H are heat, its flux, and source terms, respectively. m^H in the heat accumulation term is expressed as

$$m^H = (1-\phi)\int_{T_0}^{T} \rho_R C_R dT + \sum_J \phi S_J \rho_J e_J \ , \tag{8}$$

where ρ_R, C_R, T, and T_0 are the density and heat capacity of the porous medium, temperature and reference temperature. The heat flux is written as

$$\mathbf{f}^H = -\mathbf{K}_H \mathbf{Grad} T + \sum_J h_J \mathbf{w}_J \ , \tag{9}$$

where $\mathbf{K}_H$ is the composite thermal conductivity tensor of the porous medium.

The specific internal energy, e_J, and enthalpy, h_J, in phase J become, respectively,

$$e_J = \sum_k X_J^k e_J^k \ , \ h_J = \sum_k X_J^k h_J^k \quad . \tag{10}$$

The governing equations for geomechanics is based on the quasi-static assumption (Coussy 1995), written as

$$\mathbf{Div}\boldsymbol{\sigma} + \rho_b \mathbf{g} = \mathbf{0}\,, \tag{11}$$

where $\mathbf{Div}$ is the divergence operator, $\boldsymbol{\sigma}$ is the total stress tensor, and ρ_b is the bulk density. Tensile stress is positive in this study. The infinitesimal transformation is used to allow the strain tensor, $\boldsymbol{\varepsilon}$, to be the symmetric gradient of the displacement vector, $\mathbf{u}$,

$$\boldsymbol{\varepsilon} = \frac{1}{2}\left(\mathbf{Grad}^T\mathbf{u} + \mathbf{Grad}\,\mathbf{u}\right). \tag{12}$$

Then, considering mass, energy, linear momentum balances, we focus on non-isothermal single phase flow (i.e., gas flow) with elastoplastic geomechanics in this study, using the following constitutive relations of thermo-poro-mechanics.

Constitutive relations

We use the constitutive relations for coupled multiphase non-isothermal flow and elastoplastic geomechanics, described in Coussy (1995). For elastoplastic mechanics and nonisothermal single phase flow, the constitutive relations are written as

$$\delta\boldsymbol{\sigma} = \overbrace{\mathbf{C}_e \delta\boldsymbol{\varepsilon}_e}^{\delta\boldsymbol{\sigma}'} - \alpha\delta p_f \mathbf{1} - 3\alpha_T K_{dr}\delta T\mathbf{1}, \tag{13}$$

$$\delta\zeta_f = \alpha\delta\varepsilon_v + \frac{1}{M}\delta p_f - 3\alpha_m \delta T, \tag{14}$$

$$\delta\overline{S} = \overline{s}_f \delta m_f + 3\alpha_T K_{dr}\delta\varepsilon_v - 3\alpha_m \delta p_f + \frac{C_d}{T}\delta T, \tag{15}$$

where the subscripts *e* and *f* indicate elasticity and fluid, respectively. $\boldsymbol{\sigma}'$, K_{dr}, $\mathbf{C}_e$ are the effective stress tensor, drained bulk modulus, and drained isothermal elasticity tensor, respectively. $\mathbf{1}$ is the second order identity tensor. $\delta\zeta_f = \delta m_f / \rho_f$, where ρ_f is fluid density. α and M are Biot's coefficient and Biot's modulus in single phase fluid, written as

$$\alpha = 1 - \frac{K_{dr}}{K_s}, \quad \frac{1}{M} = \phi c_f + \frac{\alpha - \phi}{K_s}, \tag{16}$$

where K_s is the intrinsic solid grain bulk modulus, and c_f is the fluid compressibility. $3\alpha_T$ is the volumetric thermal dilation coefficient of the solid skeleton. ε_v is the total volumetric strain. $3\alpha_m = 3\alpha_{m,\phi} + 3\alpha_{m,f}$, where $\alpha_{m,\phi}$ and $\alpha_{m,f}$ are the coefficients of thermal dilation related to porosity and fluid, respectively. $\overline{S}$ and $\overline{s}_f$ are the total entropy and the specific entropy, respectively. $C_d = C_m + m_f C_{p,f}$ is the total volumetric heat capacity, where C_m is the volumetric heat capacity of the porous medium and $C_{p,f}$ is the specific heat capacity of fluid. Symbol δ denotes variation relative to the motion of the solid skeleton.

For plasticity in this study, we use the Mohr-Coulomb model, which is widely used to model failure of cohesive frictional materials. The Mohr-Coulomb model is given as

$$f = \tau'_m - \sigma'_m \sin\Psi_f - c_h \cos\Psi_f \le 0, \quad g = \tau'_m - \sigma'_m \sin\Psi_d - c_h \cos\Psi_d \le 0, \tag{17}$$

$$\sigma'_m = \frac{\sigma'_1 + \sigma'_3}{2}, \ \tau'_m = \frac{\sigma'_1 - \sigma'_3}{2}, \tag{18}$$

where $\sigma_1', \sigma_2', \sigma_3'$ are the maximum, intermediate, and minimum principal effective stresses. c_h is the cohesion. f and g are the yield and plastic potential functions, respectively. Ψ_f and Ψ_d are the friction and dilation angles, respectively. We can also rewrite a different form of the Mohr-Coulomb model as a form of the Drucker-Prager model as,

$$f = \beta_f I_1 + \sqrt{J_2} - \kappa_f \le 0, \quad g = \beta_g I_1 + \sqrt{J_2} - \kappa_g \le 0, \tag{19}$$

$$\beta_f = \frac{\sin\Psi_f}{0.5\left(3\left(1-\sin\Psi_f\right)\sin\theta + \sqrt{3}\left(3+\sin\Psi_f\right)\cos\theta\right)}, \kappa_f = \frac{3c_h}{0.5\left(3\left(1-\sin\Psi_f\right)\sin\theta + \sqrt{3}\left(3+\sin\Psi_f\right)\cos\theta\right)}, \tag{20}$$

$$\beta_g = \frac{\sin\Psi_d}{0.5\left(3\left(1-\sin\Psi_d\right)\sin\theta + \sqrt{3}\left(3+\sin\Psi_d\right)\cos\theta\right)}, \kappa_f = \frac{3c_h}{0.5\left(3\left(1-\sin\Psi_d\right)\sin\theta + \sqrt{3}\left(3+\sin\Psi_d\right)\cos\theta\right)}, \tag{21}$$

where θ is the Lode angle, written as

$$\theta = \frac{1}{3}\cos^{-1}\left(\frac{3\sqrt{3}}{2}\frac{J_3}{J_2^{3/2}}\right). \tag{22}$$

I_1, J_2, and J_3 are invariants of the effective stresses as follows

$$I_1 = \mathbf{tr}\boldsymbol{\sigma}', J_2 = \frac{1}{2}\mathbf{s}':\mathbf{s}', J_3 = \det\mathbf{s}', \text{where } \mathbf{s}' = \boldsymbol{\sigma}' - \frac{I_1}{3}\mathbf{1}, \tag{23}$$

where **tr** is the trace of a second order tensor. Fig. 1 shows the comparison between the Drucker-Prager and Mohr-Coulomb models.

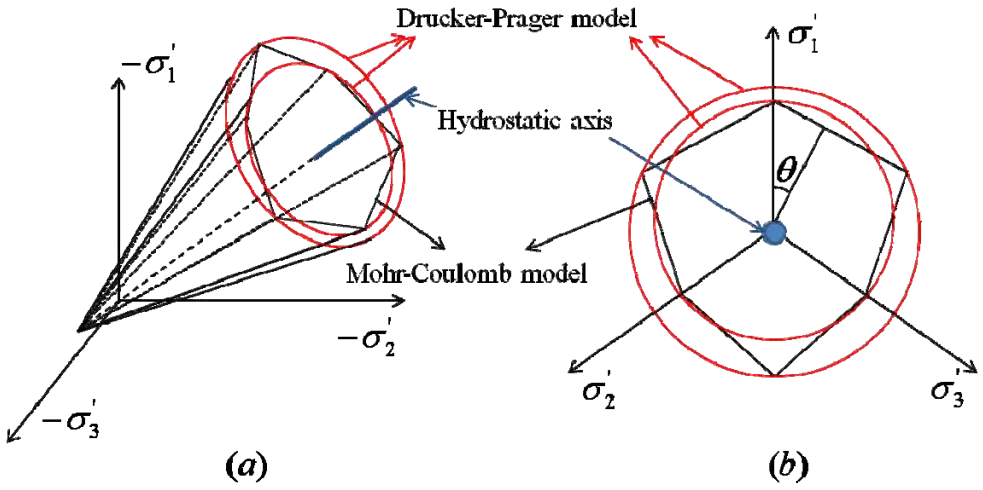

Fig. 1. The yield surfaces of the Drucker-Prager and Mohr-Coulomb models on (a) the principle effective stress space and (b) on the deviatoric plane. In elastoplasticity, all the effective stresses are located inside or on the yield surfaces.

Note that the coefficients of Drucker-Prager model used in this study (i.e., Eqs. (20) and (21)) are adjusted to the Mohr-Coulomb model, and the two models have the same yield and potential functions. In this study, when modeling the Mohr-Coulomb model, we make use of an algorithm of the Drucker-Prager model, a I_1 - J_2 plasticity model, treating the coefficients of the Drucker-Prager model explicitly but dynamically (i.e., the coefficients associated with J_3).

When material failure occurs, micro-fractures are created and connected, making macroscopic fractures. As a result, permeability can increase dramatically and discontinuously in time. We then consider the change in permeability, using a permeability (or transmissibility) multiplier ω_p, as

$$\omega_p \begin{cases} =1 & \text{if not failed} \\ >>1 & \text{if failed} \end{cases}, \tag{24}$$

by which the intrinsic permeability, k_0, is expressed as $k_0 = \omega_p k_m$, where k_m is the intact rock permeability. Thus, the permeability is a step function for a failure status. In this study, we simply use $\omega_p = 10^2$ when the intact rock faces failure. One may use other complicated models for ω_p for the further accuracy of certain specific reservoirs.

Numerical implementation

We use the finite volume and finite element methods for flow and geomechanics in space discretization, respectively, which are widely used in reservoir and geotechnical engineering, respectively (Aziz and Settari 1979; Lewis and Schrefler 1998; Hughes 2000). This mixed-space discretization can provide advantages such as local mass conservation and better numerical stability in space, compared with the finite element method for both flow and geomechanics (Jha and Juanes 2007; Kim et al. 2011a,b).

For time discretization, we use the backward Euler method, which is typically used in reservoir simulation. We use TOUGH+RealGasH2O as a fluid and heat flow simulator and ROCMECH for a geomechanics simulator, namely T+M, recently developed in the Lawrence Berkeley National Laboratory (Kim and Moridis, 2013).

When we solve coupled problems numerically, there are two approaches; fully coupled (monolithic) and sequential methods. The fully coupled methods solve the coupled problems simultaneously, using the Newton-Raphson method (Lewis and Sukirman, 1993a,b; Sukirman and Lewis, 1993; Pao et al., 2001; Gutierrez and Lewis, 2002; Pao and Lewis, 2002; Lewis et al., 2003; White and Borja, 2008). This approach typically provides unconditional stability, but requires a unified flow and geomechanics, which results in the enormous software development and huge computational cost. On the other hand, the sequential methods can offer the use of existing robust flow and geomechanics simulators only by constructing an interface between them (Armero and Simo, 1992, 1993; Settari and Mourits, 1998; Armero 1999). This provides wide flexibility and high efficiency for code management, but may be limited by numerical stability and accuracy, which are the main issues in using the sequential methods. According to Kim et al. (2011b), among several sequential methods, the fixed stress sequential method can provide unconditional stability and high accuracy, comparable to the fully coupled methods. The fixed-stress method solves the flow problem, fixing the total stress field, where the strain and displacement fields can be changed, and calculating the contribution of geomechanics to flow explicitly. Then, it solves geomechanics, based on the solutions obtained at the previous flow problem. This sequential method can easily be implemented by the Lagrange porosity function Φ and its correction $\Delta\Phi$ (Settari and Mourits, 1998; Kim et al., 2012a), written as a form of the staggered approach as,

$$\Phi^{n+1} - \Phi^n = \underbrace{\left(\frac{\alpha^2}{K_{dr}} + \frac{\alpha - \Phi^n}{K_s} \right)}_{\Phi^n c_p} (p^{n+1} - p^n) + 3\alpha_T \alpha (T^{n+1} - T^n) - \underbrace{\left(\sigma_v^n - \sigma_v^{n-1} \right)}_{\Delta\Phi}, \tag{25}$$

where c_p is the pore compressibility in conventional reservoir simulation (Aziz and Settari, 1979), and σ_v is the total volumetric mean stress. Φ is defined as the ratio of the pore volume in the deformed configuration to the bulk volume in the reference (initial) configuration. The porosity correction term, $\Delta\Phi$, is calculated from geomechanics, which corrects the porosity estimated from the pore compressibility. The fixed-stress sequential method solves two-way coupling between flow and geomechanics, so it captures the Mandel-Cryer effects, solving Mandel's problem correctly, which cannot be simulated by the uncoupled simulation (Kim and Moridis, 2013). For further verification, Fig. 2 shows that T+M matches the analytical solution of McNamee and Gibson (1960a,b), where the pressure rise-up at early times can only be matched by the two-way coupled approach. The right of Fig. 2 shows number of iteration when the fixed-stress method takes full iteration, where the porosity correction is applied to iteration level, instead of time level. This full iteration provides the same solution as the monolithic (fully coupled) method. During simulation, only 3 iterations for convergence were taken almost all every time steps, except at early times. This fast convergence was originally investigated by Kim et al. (2011b) with a priori mathematical analysis and numerical simulation. In this study, we use the staggered approach of the fixed stress method, because it provides accurate solutions with efficiency, comparable to the fully coupled method.

When implementing the Mohr-Coulomb model, we reference the algorithms proposed by Wang et al. (2004). For the Mohr-Coulomb model, we may face numerical instability at the discontinuous corners (Borja et al., 2003; Wang et al., 2004).

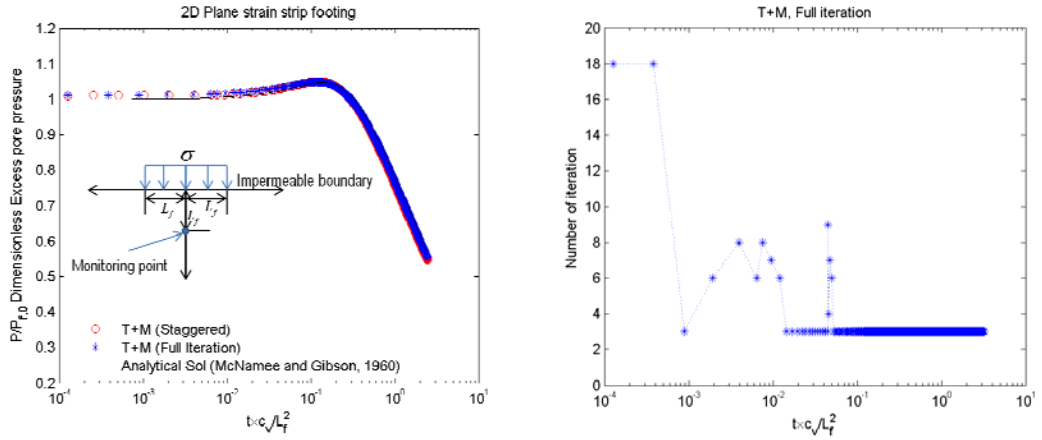

Fig. 2. Verification test of two-way coupling between flow and geomechanics. $P_{f,0}$ is the instantaneous pressure build-up at the initial time. t , c_v , and $\overline{\sigma}$ are time, the consolidation coefficient, and geomechanical loading, respectively. T+M matches the analytical solution of McNamee and Gibson (1960a,b), capturing the Mandel-Cryer effect. The staggered fixed-stress method provides high accuracy with efficiency. The fixed-stress method yields fast convergence when it takes full iteration, where tolerance is $\left|(P^k - P^{k-1})/P_i\right|_{\mathbf{x}=\mathbf{x}_0} < 10^{-5}$. The superscript k indicates the iteration level. P_i and $\mathbf{x}_0$ are the initial pressure and the monitoring point, respectively.

Numerical examples

We perform two test cases for 2D gas flow simulation coupled to plane strain geomechanics, which are aimed at gas production from tight gas or shale gas reservoirs with several uniform long horizontal wells. These production scenarios can reduce a 3D system to 2D because of symmetry (e.g., a half domain between the wells (or primary fractures)) and the plane strain condition, as shown in Fig. 3. Cases 1 and 2 contain vertical and horizontal fractures, respectively. There are six monitoring points: P1 (x=23.77m, z=-58.5m) and P2 (x=33.77m, z=-58.5m) for Case 1, and P3 (x=29.5m, z=-74.03m), P4 (x=47.5m, z=-74.03m), P5 (x=29.5m, z=-61.265m), and P6 (x=49.5m, z=-61.265m) for Case 2, respectively. The monitoring points are chosen to show flow and geomechanics responses of the areas away from the primary fractures.

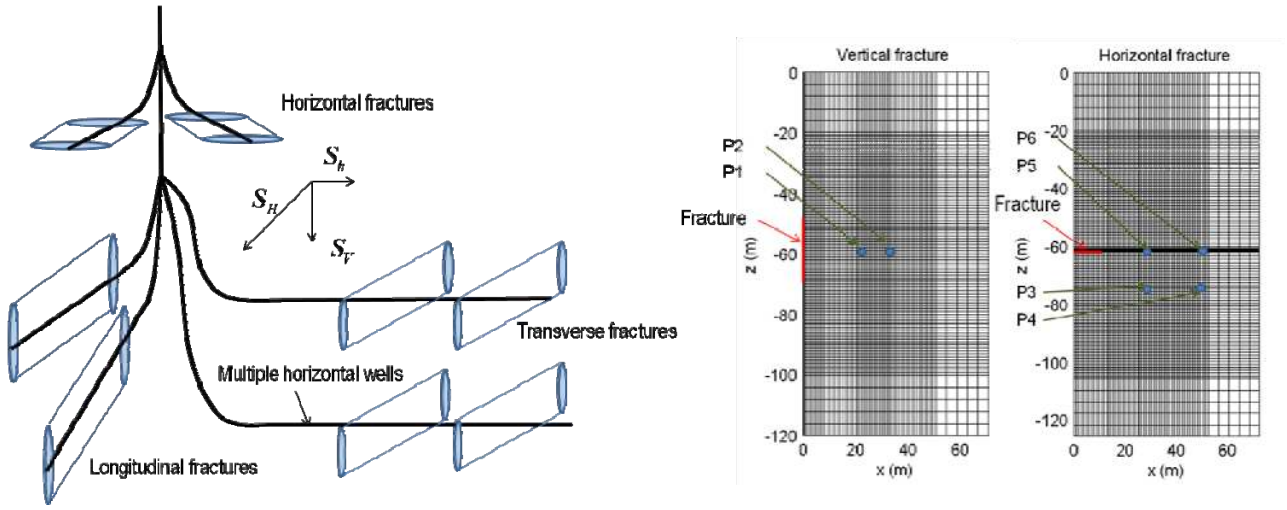

Fig. 3. A schematic diagram of gas production with horizontal wells (left) and discretized domains that contain vertical and horizontal primary fractures (right). Production scenarios with several long uniform horizontal wells in 3D can be reduced to 2D systems using symmetry and plane strain geomechanics. The meshes of the domains are refined around the fractures.

For Case 1, the reservoir domain is divided into 61×90 gridblocks in horizontal and vertical (x, z) directions. Vertically, we have uniform grid sizes, $\Delta z = 1.0m$ between the 6th and 85th horizontal layers, and $\Delta z = 4.0m$ in the other layers. On the other hand, in the horizontal direction, we have a 0.01m grid size of the first vertical grid layer that contains a vertical primary fracture whose aperture is 0.01m, non uniform sizes that are 0.02m, 0.04m, 0.08m, 0.16m, 0.32m, 0.64m from the second to

the 7th vertical grid layers, a uniform grid size that has $\Delta x = 1.0m$ from the 8th to the 56th vertical grid layers, and $\Delta x = 4.0m$ from the 57th to the last vertical layers. The length of the vertical fracture, where the production well is located at (x=0.005m, z=-60.5m), is 20m.

For Case 2, the 2D reservoir domain is divided into 57×106 gridblocks in horizontal and vertical (x, z) directions. Horizontally, we have a uniform grid size, $\Delta x = 1.0m$ from the first to the 52th vertical layers and $\Delta x = 4.0m$ from the 53th to the last vertical layers. On the other hand, in the vertical direction, we have a uniform grid size that has $\Delta z = 4.0m$ from the first to the 5th horizontal grid layers, a uniform grid size that has $\Delta z = 1.0m$ from the 6th to the 45th horizontal layers, non uniform sizes that are 0.64m, 0.32m, 0.16m, 0.08m, 0.04m, 0.02m from the 46th to the 51th horizontal grid layers, a horizontal primary fracture whose aperture is 0.01m at the 52th horizontal grid layer, non uniform sizes that are 0.02m, 0.04m, 0.08m, 0.16m, 0.32m, 0.64m from the 53th to the 58th horizontal grid layers, a uniform grid size that has $\Delta z = 1.0m$ from the 59th to the 101th horizontal grid layers, and a uniform grid size that has $\Delta z = 4.0m$ from the 102th to the last horizontal layers. The length of the horizontal fracture, where the production well is located at (x=0.5m, z=-61.265m), is 10m.

For both cases we have the same initial and boundary conditions for flow and geomechanics. For flow, we have no flow at the boundaries. The initial pressure is 68.95MPa with no gravity. The initial temperature is $176.67^{o}C$. The heat capacities of the porous media, and the wet and dry thermal conductivities for all layers are $1000\,Jkg^{-1\,o}C^{-1}$, $3.1\,Wm^{-1\,o}C^{-1}$, and 0.5 $Wm^{-1\,o}C^{-1}$, respectively. We apply a constant bottom hole pressure at the production well, 20MPa. The initial permeabilities for the primary fractures and intact rock (rock matrix) are $2.556 \times 10^{-13}\,m^2$ and $8.645 \times 10^{-18}\,m^2$, respectively, where 1 Darcy is $9.87 \times 10^{-13}\,m^2$. The initial porosities for them are 1.0 and 0.1, respectively. For geomechanics, we have no horizontal displacement at both sides, based on symmetry shown in Fig. 3, and no displacement at the bottom. The overburden at the top is $\bar{\sigma} = 68.95$MPa. The initial vertical and horizontal principal stresses are -68.95MPa. Young's moduli for the fractures and rock matrix are 185MPa and 1.282GPa, respectively, and Poisson's ratios for them are 0.0 and 0.22, respectively. For both materials, the Biot coefficients, α, are 1.0, the bulk densities are $2600\,kg \cdot m^{-3}$, and the thermal dilation coefficients are $1.0 \times 10^{-5\,o}\,C^{-1}$. The cohesion, friction and dilation angles for shear failure are 4.0MPa, $\Psi_f = 28.6^0$ (0.5rad) and $\Psi_d = 28.6^0$ (0.5rad) for the both materials. Table 1 summarizes the main initial input data of flow and geomechanical properties of the rock matrix. We use generalized reservoir models, rather than selecting geomechanical properties for a certain specific reservoir. The geomechanical properties used in this study are within a range of the properties of shale gas reservoirs (Eseme et al., 2007; Sondergeld et al., 2010). We take relatively low Young's modulus of intact rock, compared with typical shale gas reservoirs, assuming that high temperature lowers Young's modulus of shales (Eseme et al., 2007). We also use low Young's modulus for the primary fracture because the fracture is typically much deformable than intact rock (e.g., Nguyen and Abousleiman (2010)). We will investigate flow and geomechanical responses for the above reference cases as well as test cases where different values of Biot's coefficient, bottom hole pressure, friction and dilation angles, horizontal well spacing, and initial conditions are used.

Table. 1 Initial data for flow and geomechanical properties of the rock matrix

Initial pressure	68.95MPa	Young's modulus	1.282GPa
Initial temperature	$176.67^{o}C$	Poisson's ratio	0.22
Initial porosity	0.1	Cohesion	4MPa
Initial permeability	$8.76 \times 10^{-4}\,mD$	Friction & dilation angles	28.6^{o}
Biot's coefficient	1.0	Thermal dilation coefficient	$1.0 \times 10^{-5\,o}\,C^{-1}$

Elasticity

We first perform numerical simulations for Cases 1 and 2 on the basis of elasticity. The simulations can indicate the potential areas of failure during gas production. Let us introduce λ in order to indicate the distance between the effective stresses and the yield function of the Mohr Coulomb model, written as

$$\lambda = \frac{\tau'_m - \sigma'_m \sin\Psi_f - c_h \cos\Psi_f}{\sqrt{\sin^2\Psi_f + 1}}. \tag{26}$$

High values indicate potential areas of shear failure, and failure can occur when $\lambda > 0$. Fig. 4 shows distributions of λ for Cases 1 and 2, using elasticity, after 75 days. The effective shear stresses are concentrated at the right boundaries because of the horizontally constrained boundary condition, especially around the top and center of the right side boundary, resulting in high values of λ. This implies that gas production can cause failure away from the production well. This failure may be beneficial to increase permeability in tight gas or shale gas reservoirs, but it could be problematic if surface facilities exist, or weak geological sealing occurs, in the vicinity of the failure area. In this study, we focus on productivity of the gas reservoirs,

investigating changes in permeability, failure, and flow and geomechanical variables.

Plasticity

We perform failure analyses for Cases 1 and 2, using the Mohr-Coulomb model. For Case 1, Fig. 5 shows propagation of the region where permeability increases due to shear failure. The areas that have non-zero in the figure experienced plasticity during simulation. Specifically, the value indicates the number of Gauss points within a gridblock which faced plasticity. The region initially propagates from the fracture tips at top and bottom. As gas production goes on, failure also occurs around the center of the domain, independent from the fracture propagation near the fracture tips. Then failure propagates from the center of the domain to the middle of the right boundary.

In Fig. 6(a), the effective stresses at P1 and P2 propagate straight toward the yield function at early times. Then, the effective stresses at P1 and P2 enter plasticity and then return to elasticity. This behavior mainly results from failure and enhancement of permeability in other areas, followed by redistribution in fluid pressure and effective stress. In Fig. 6(b), we compare gas production rates between elasticity and plasticity, which shows that gas production with plasticity yields higher production rate than that with elasticity, because the failure creates high permeability areas. In Fig. 6(c), we observe non-smooth evolution in pressure at P1 and P2. In particular, when failure occurs at P2, pressure at P1 suddenly increases, being connected to the enhanced permeability region where pressure is higher, including P2. After the sudden pressure peak at P1, the pressure decreases again because of fast pressure diffusion due to high permeability. In Fig. 6(d), we find that the time of the permeability increase at P2 is almost identical to the time of the peak pressure at P1. The pressure increase at P2 is found after 60 day, because other areas experienced failure, affecting pressure at P2, just like P1.

For Case 2, failure occurs near the fracture tip, as shown in Fig. 7. At early times, the fracture propagates, creating two (upper and lower) branches. Then, the failed areas spread widely at both upper and lower parts, enhancing permeability. Fig. 8(a) shows that the effective stresses at P3 and P4 propagate toward the yield function, entering plasticity and then returning to elasticity, similar to those for Case 1. In Fig. 8(b), the production rate with plasticity is higher than that with elasticity. From Fig. 8(d), we observe that failure at P3 occurs earlier than at P4. As a result, as shown in Fig. 8(c), the pressure peak at P3 around 35day is found because of the sudden increase of permeability.

From the results of Figs. 5-8, we find significant nonlinearity and complexity, when using stress dependent permeability in conjunction with plasticity, which considerably changes permeability fields dynamically. This behavior cannot properly be simulated by the conventional flow-only or uncoupled simulation. We use Figs 5-8 as the references cases, which will be compared with the tests cases in which we take different flow and geomechanical properties and production scenarios as follows.

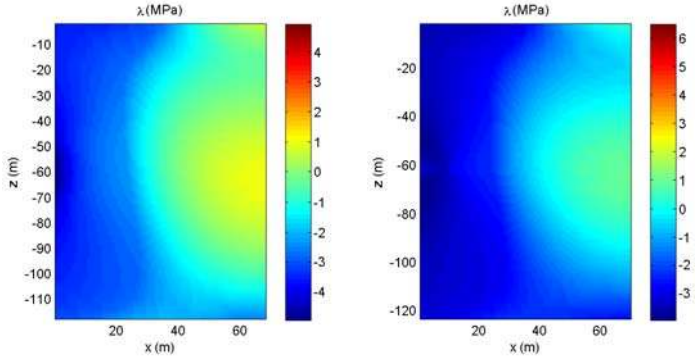

Fig. 4. Distributions of values of λ for Case 1 (left) and Case 2 (right) from numerical simulation of elasticity. The term λ indicates the possibility of failure of the Mohr-Coulomb model. When $\lambda > 0$, the effective stresses from elasticity are located out of the yield function. Failure is shown to be possible for the areas near the right boundaries, away from the production wells for both cases.

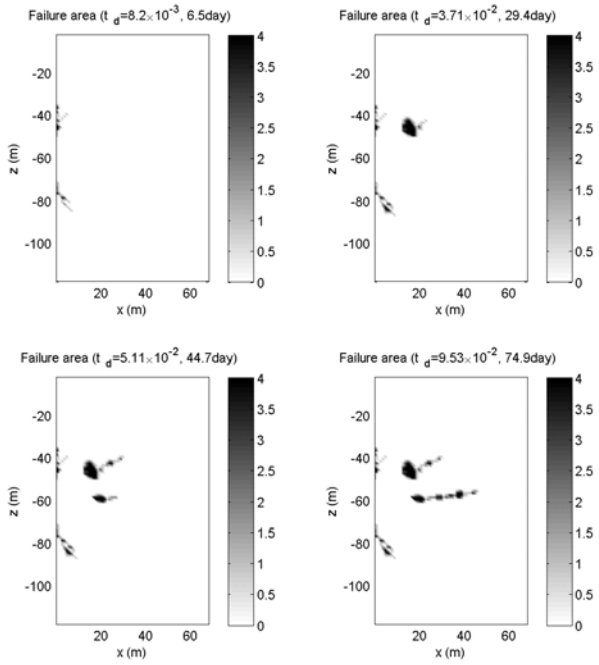

Fig. 5. Evolution of areas of the enhanced permeability by shear failure for Case 1. During gas production, the enhanced permeability areas increase due to the failure. Some areas returned to elasticity, after experiencing plasticity because of redistribution of fluid pressure, but they have the permanent enhanced permeability. $P_d = p / p_b$ **and** $t_d = k_{m,0} t / (\phi_{m,0} c_t \mu_g L_x L_z)$**, where** p_b **is the bottom hole pressure.** $k_{m,0}$**,** $\phi_{m,0}$**,** L_x**, and** L_z **are the initial rock matrix permeability and porosity, and the horizontal and vertical lengths of the domain, respectively.** c_t **is the total compressibility used for the flow simulation.**

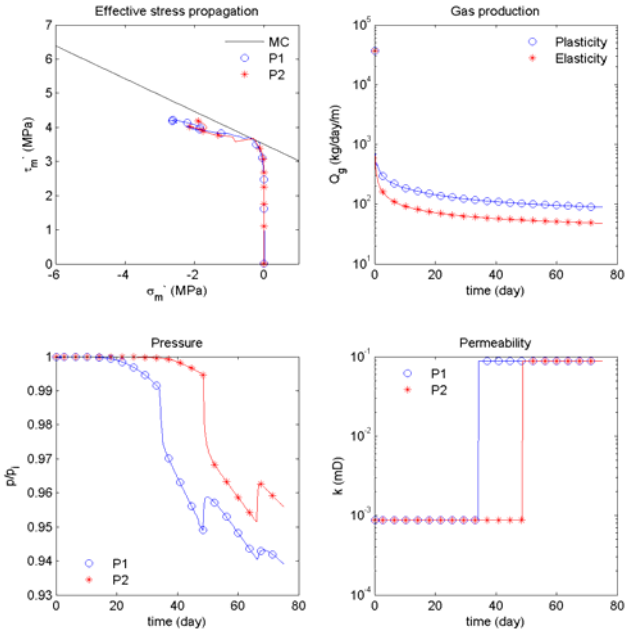

Fig. 6. (a) Evolution of effective stresses (a), (b) comparison of production rates between plasticity and elasticity, (c) evolution of pressures at P1 and P2, and (d) evolution of permeability for Case 1. 'MC' indicates the Mohr-Coulomb yield function. The effective stresses at P1 and P2 face failure and then return to elasticity. Due to the failure, permeability of the reservoir increases, yielding higher productivity.

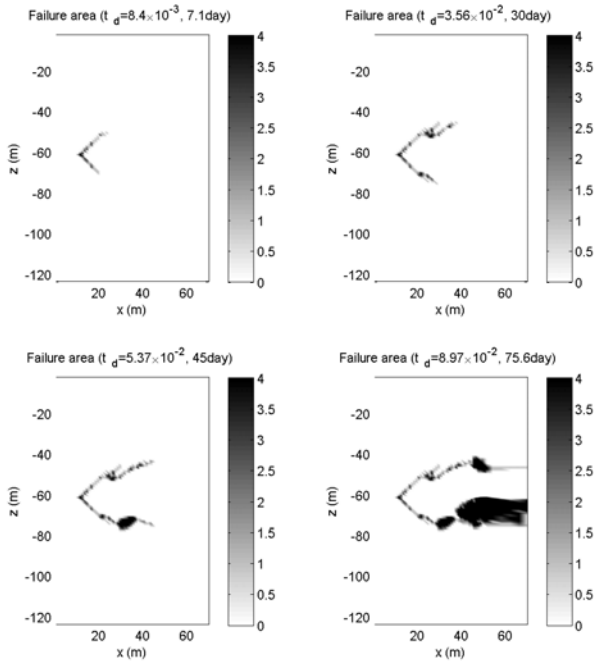

Fig. 7. Evolution of the areas of the enhanced permeability by shear failure in Case 2. During production, these areas increase because of the failure, just as was observed in Case 1.

Effect of Biot's coefficient We reduce Biot's coefficient from 1.0 to 0.8, because some reservoirs have lower Biot's coefficients than 1.0 (Zoback, 2007). The lower Biot's coefficient, the less contribution of fluid pressure to effective stress in geomechanics. In Fig. 9, we find much smaller failure areas for both Cases 1 and 2, compared to the reference cases. When Biot's coefficient is low, the poromechanical effects become low, from which the pressure change causes less perturbation in the geomechanical system.

Effect of the bottom hole pressure We increase the bottom hole pressure from 20MPa to 30MPa, where Biot's coefficient is 1.0. This fundamentally decreases the geomechanical loading to the reservoirs. As a result, we obtain much smaller areas of enhanced permeability, as shown in Fig. 10. In this figure, we only observe small fracture propagation near the primary fracture tips. Thus, sufficient perturbation in the geomechanics system through the pressure change is required in order to create sufficient areas of enhanced permeability. Hydraulic fracturing is also based on the same idea that the increase of fluid pressure can create a fracture, inducing tensile failure and opening the fracture. Difference between hydraulic fracturing processes and failure during gas production lies in ways of geomechanical perturbation (i.e., the increase and decrease of fluid pressure, respectively).

Effect of properties of the plastic model We modify the friction and dilation angles from $\Psi_f = \Psi_d = 28.6^0$ (0.5rad) to $\Psi_f = \Psi_d = 20.1^0$ (0.35rad), keeping 30MPa of the bottom hole pressure. A lower friction angle implies a lower slope of the failure line on the σ_m' and τ_m' plot. Thus, failure can occur more easily. For Case 1, Figs. 11(a) and 11(b) show large areas of enhanced permeability although the bottom hole pressure is 30MPa, when compared with Fig. 10. We also observe that failure occurs not only at the fracture tips but also parallel with the primary fracture. Then more enhanced reservoir yields almost the same production rate as the reference case, as shown in Fig. 11(c). In Fig. 11(d), we find the sudden jump of pressure at P1 around 60 day, because of failure. As failure proceeds during simulation, the permeability field changes discontinuously because permeability is a discontinuous function of the failure status. From this discontinuity, the responses in pressure are not smooth. For Case 2, we obtain similar results. Compared with Fig. 10, Figs. 12(a) and 12(b) show much larger failure areas, enhancing the reservoir permeability. The fracture propagates with two branches toward the right boundary, mainly from the upper branch. Due to large failure, the production rate is comparable to that of the reference case, shown in Fig. 12(c), and pressure decreases noticeably within the reservoir (Fig. 12(d)).

Effect of spacing between the horizontal wells We reduce the horizontal domains from 70.27m to 58.27m for Case 1, and from 72m to 60m for Case 2, shortening 12m for both cases. This implies that two horizontal wells are closer, compared with

the reference cases. We keep 30MPa of the bottom hole pressure, higher than that of the reference cases. In Fig. 13, we find that secondary fracturing occurs faster for both cases, making larger areas of enhanced permeability, when compared with Fig. 10. Faster fracturing is mainly due to the heaving effects and well interference, which are realized as the boundary effects in numerical simulation.

Effect of different initial total stress and pressure distributions We change the initial conditions of the reference cases, having two sets of different initial total principal stresses and 53.95MPa of initial reservoir pressure. We also take 3.0MPa and 5.0MPa of cohesions for the primary fractures and rock matrix, respectively. Other conditions are the same as those of the reference cases. We apply -55.16MPa, -62.06MPa, -68.95MPa of initial total stresses in the x, y, z directions, respectively to Figs. 14(a) and 14(b), and -68.95MPa, -62.06MPa, -55.16MPa to Figs. 14(c) and 14(d). Those different total stresses yield non-zero effective stresses at initial time. In Figs. 14(a) and 14(b), shear failure propagates horizontally for Cases 1 and 2, when overburden is higher than side burden. On the other hand, Figs. 14(c) and 14(d), shear failure propagates vertically, when overburden is lower than side burden. Then shear failure induced by fluid production shows different directions of fracture propagation from tensile failure of hydraulic fracturing induced by fluid injection. In addition, when Figs. 14(a) and 14(b) are rotated by 90 degree, their directions of fracture propagation are almost the same as those of Figs. 14(c) and 14(d), because initial total stresses conditions of Figs. 14(a) and 14(b) after the rotation are the same as those of Figs. 14(c) and 14(d).

Effect of the porosity change Fig. 15 shows propagation of secondary fractures without consideration of the porosity change (i.e., constant porosity). When comparing Fig. 15 with Figs. 5 and 7, we find differences between with and without the porosity change, especially for Case 2, even though the directions of the fracture propagation between the two are similar. In Fig. 7, both upper and lower branches were developed, while the upper branch was mainly developed, shown in the left of Fig. 15. Thus, the two-way coupled poromechanics needs to be considered for better accuracy.

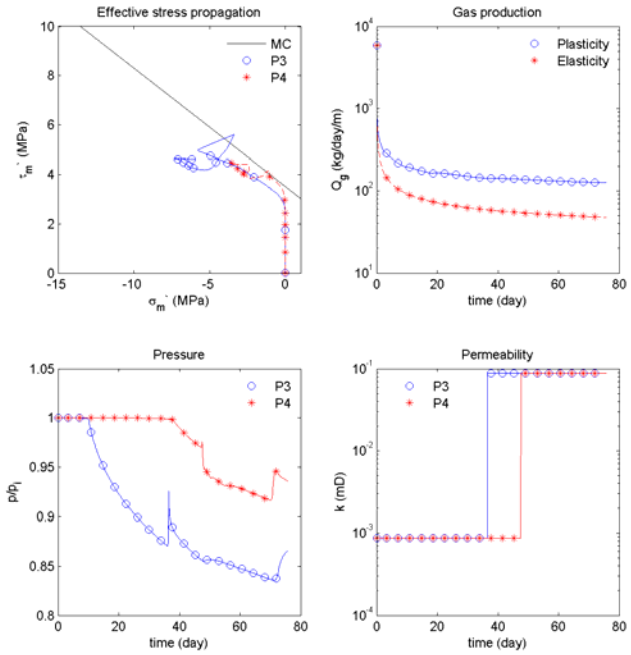

Fig. 8. (a) Evolution of effective stresses, (b) comparison of production rates between elasticity and plasticity, (c) evolution of pressures at P3 and P4, and (d) evolution of permeability at P3 and P4. P3 and P4 face failure and return to elasticity, similar to Case 1. Failure enhances permeability, followed by the production rate. The pressures at P3 and P3 decrease fast because of shear failure followed by enhancement of permeability.

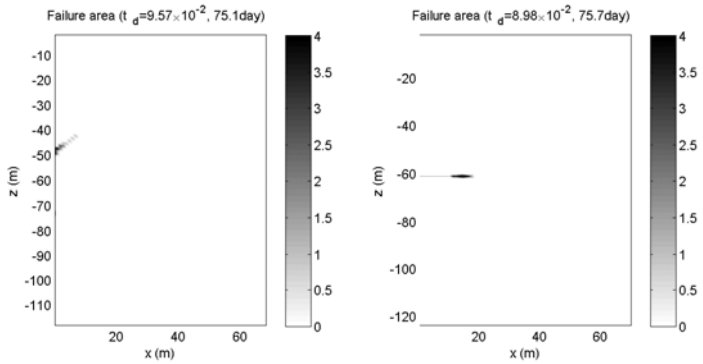

Fig. 9. The areas of the enhanced permeability induced by plasticity for Case 1 (left) and Case 2 (right), when Biot's coefficient is 0.8. Compared with the reference cases, 0.8 of Biot's coefficient causes less failed zones, because a lower Biot' coefficient less contributes to perturbation in the geomechanical system.

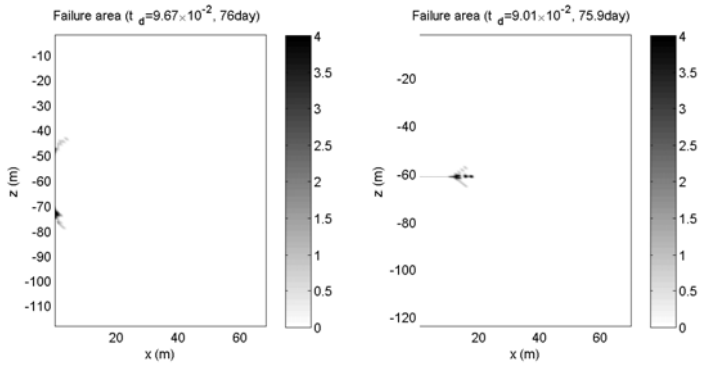

Fig. 10 The areas of enhanced permeability for Case 1 (left) and Case 2 (right), when the bottom hole pressure is 30MPa. The failure areas for both cases are located only near the primary fracture tips, much smaller than those of 20MPa of the bottom hole pressure. Lower geomechanical loading induces smaller failure areas, less activating the primary fractures.

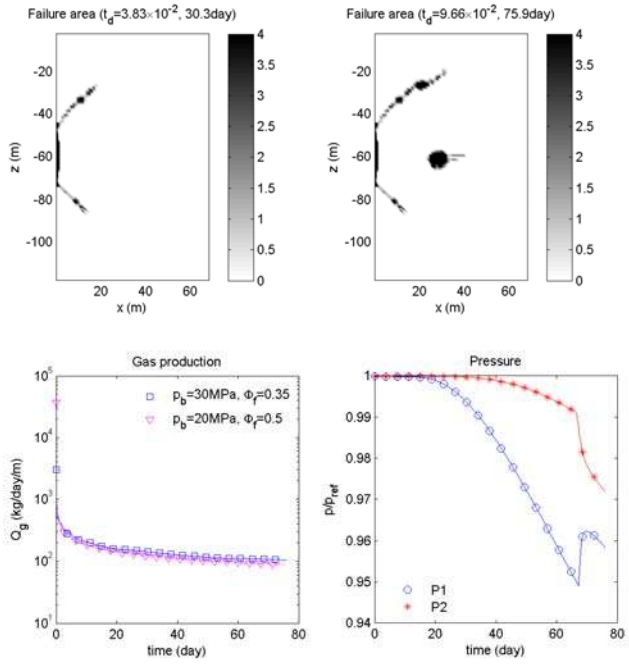

Fig. 11. Fracture propagation for Case 1 ((a) and (b)), (c) comparison of the production rates between and $P_b = 30MPa, \Phi_f = 0.35$ and $P_b = 20MPa, \Phi_f = 0.5$, and (d) evolution of pressure at P1 and P2. Fracturing is enhanced more, compared with Fig. 10, because of a lower slope of the failure line.

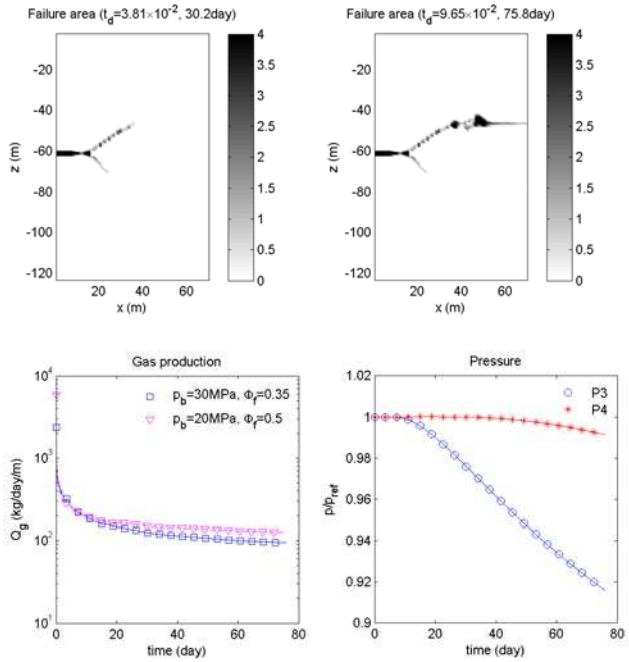

Fig. 12. Fracture propagation for Case 2 ((a) and (b)), (c) comparison of the production rates between and $P_b = 30MPa, \Phi_f = 0.35$ and $P_b = 20MPa, \Phi_f = 0.5$, and (d) evolution of pressure at P3 and P4. Fracturing is enhanced more, compared with Fig. 10, similar to Case 1.

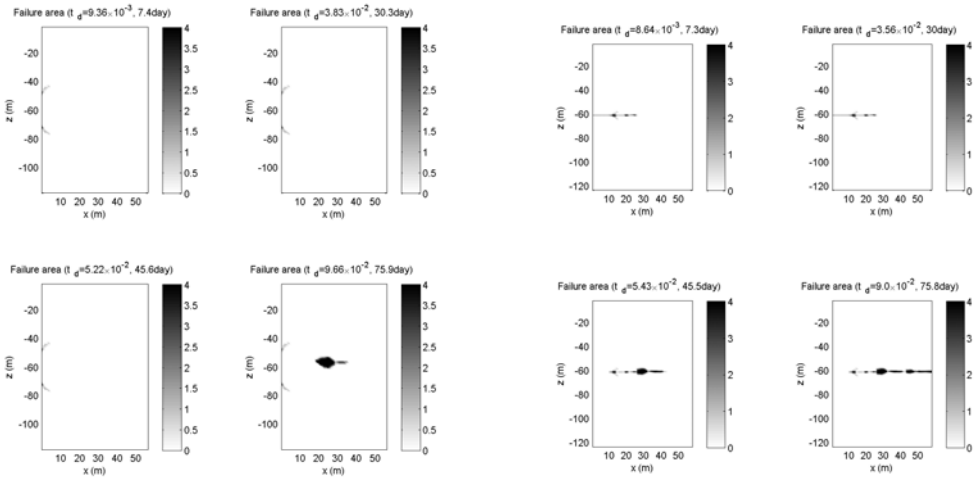

Fig. 13 Fracture propagation for Case 1 (left) and Case 2 (right). Secondary fracturing occurs faster in large areas for both cases.

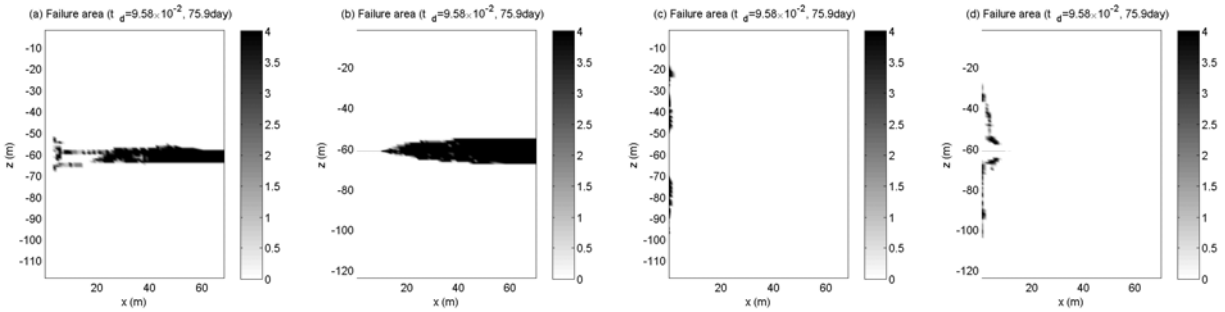

Fig. 14 Fracture propagation for two sets of different initial total stresses. For both Cases 1 and 2, shear failure induced by production propagates horizontally when overburden is higher than side burden ((a) and (b)), while it propagates vertically when side burden is higher than overburden ((c) and (d)).

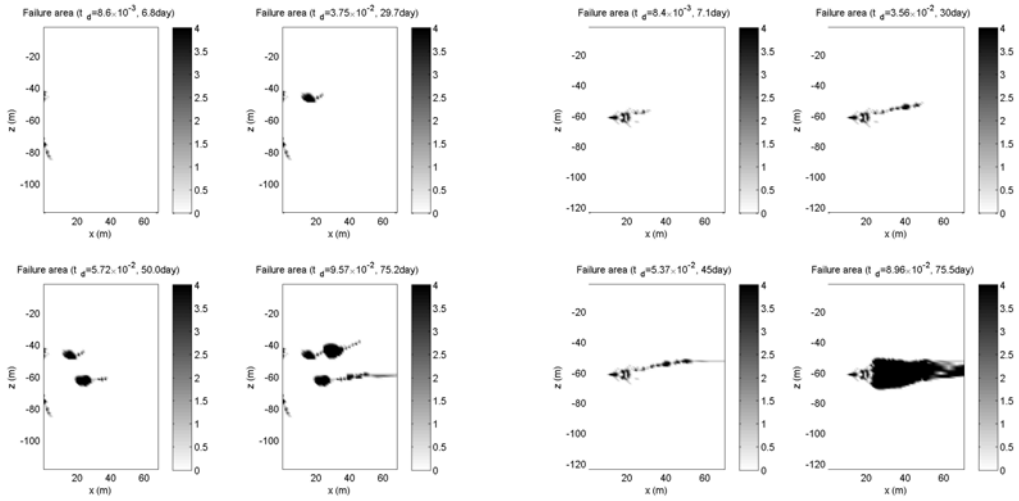

Fig. 15 Fracture propagation without consideration of the porosity change (i.e., constant porosity during simulation) for Case 1 (left) and Case 2 (right). Comparing Figs. 5 and 7, we find differences between with and without poromechanical effects in flow, particularly for Case 2.

Dynamic double porosity model

Failure implies creation of fractures, which take small volume when compared with intact rock, and the theory of single porosity has significant limitation not only in coupled flow and geomechanics also in flow-only simulations because the single porosity might not properly represent two distinct materials such as the fracture and intact rock (Bai 1999; Barenblatt et. al. 1960; Pruess and Narasimhan 1985). To solve this issue, the double porosity (or more generally multiple porosity model) has been introduced for more realistic simulation, representing local heterogeneity (Barenblatt et al.1960; Pruess and Narasimhan 1985; Berryman 2002; Bagheri and Settari 2008). The fracture-rock matrix systems based on the double porosity model are representative of any composite systems that consist of a high permeable material transporting fluid over the domain and the other materials storing fluid and conveying it to the high permeable material. In this sense, the double porosity model can be well suited for flow for fractured reservoirs.

We modify the constitutive relations for the multiple porosity model in thermoporomechanics proposed by Kim et al. (2012b), extended from the relations by Berryman (2002). We do not use the Einstein notation in this section for clarity. Then, the constitutive relations for the double porosity model such as a fracture-rock matrix system are written as

$$\delta\boldsymbol{\sigma} = \overbrace{\mathbf{C}_{up}\delta\boldsymbol{\varepsilon}}^{\delta\boldsymbol{\sigma}'} - \sum_l b_l^* \delta p_l \mathbf{1} - \sum_l \tilde{b}_l^* \delta T_l \mathbf{1},\ b_l^* = -K_{dr} b_l,\ \tilde{b}_l^* = -K_{dr}\tilde{b}_l, \tag{27}$$

$$\delta\zeta_l = b_l^* \delta\varepsilon_v + \sum_m L_{l,m}^{-1} \delta p_m\ , \tag{28}$$

where the subscript *l* indicates a material (sub-element) within a gridblock. K_{dr} and $\mathbf{C}_{up}$ are the upscaled elastoplastic drained bulk and tangent moduli at the level of the gridblock, respectively. b_l^* and $\tilde{b}_l^*$ are the coupling coefficients. b_l , $\tilde{b}_l$, K_{dr}, $L_{l,m}^{-1}$ are written as

$$b_l = -\frac{\alpha_l \eta_l}{K_l},\ \tilde{b}_l = -3\alpha_{T,l}\eta_l,\ K_{dr} = \sum_l \frac{\eta_l}{K_l},\ \mathbf{L}^{-1} = \begin{bmatrix} \eta_f N_f & 0 \\ 0 & \eta_M N_M \end{bmatrix}, \tag{29}$$

where α_l, $\alpha_{T,l}$, η_l, and K_l are Biot's coefficient, thermal dilation coefficient, volume fraction, and the drained bulk modulus for material *l,* respectively. $L_{l,m}(\equiv \mathbf{L})$ represents the Biot modulus matrix of the double porosity model (e.g., the fracture-rock matrix system), where N_f and N_M are the inverse of the Biot moduli, M_f and M_M, for the fracture and rock matrix media, respectively, (i.e., $N_f = 1/M_f$ and $N_M = 1/M_M$). The subscripts *f* and *M* indicate the fracture and rock matrix, respectively.

For naturally fractured reservoirs, the double porosity model is used initially, while, in this study, we change the single porosity model into the double porosity during simulation every time when a material faces plasticity. Thus, for the naturally fractured reservoirs, $\mathbf{C}_{up}$ and K_{dr} at a gridblock are obtained from an upscaling from given properties of fracture and rock matrix materials. Accordingly, the return mapping for elastoplasticity is performed at all the subelements (Kim et al., 2012b).

In this study, however, $\mathbf{C}_{up}$ and K_{dr} are directly obtained from the elastoplastic tangent moduli at a gridblock (global) level, not the subelements, while we need to determine the drained bulk moduli of fracture and rock matrix materials for the double porosity model, followed by the coupling coefficients. To this end, we assume that the rock matrix has the same drained bulk modulus as that of the single porosity material before plasticity (i.e., elasticity), because the rock matrix is undamaged. Then, from Eq. 29_3, the drained bulk modulus of the fracture medium can be determined as

$$K_f = \eta_f \frac{K_{dr} K_M}{K_M - K_{dr}(1-\eta_f)}. \tag{30}$$

Considering K_{dr} and K_f to be positive for wellposedness, the volume fraction of the fracture medium, η_f, has the constraint as

$$\eta_f > 1 - \frac{K_M}{K_{dr}}. \tag{31}$$

Then, according to Kim et al. (2012b), Lagrange's porosity for material *l* can be written as

$$\delta\Phi_l = \left(\frac{\alpha_l^2}{K_l} + \frac{\alpha_l - \Phi_l}{K_s}\right)\delta p_l + 3\alpha_{T,l}\alpha_l \delta T_l - \frac{b_l}{\eta_l}\delta\sigma_v, \tag{32}$$

from which, the modified fixed stress split of the double porosity system yields

$$\Phi_l^{n+1} - \Phi_l^n = \left(\frac{\alpha_l^2}{K_l} + \frac{\alpha_l - \Phi_l^n}{K_s}\right)\left(p_l^{n+1} - p_l^n\right) + 3\alpha_{T,l}\alpha_l\left(T_l^{n+1} - T_l^n\right) - \underbrace{\frac{b_l}{\eta_l}\left(\sigma_v^n - \sigma_v^{n-1}\right)}_{\Delta\Phi_l}, \tag{33}$$

where σ_v is the total volumetric mean stress at the gridblock. The permeability (or transmissibility) multiplier for the fracture $\tilde{\omega}_p$ in the double porosity system can be given as $\tilde{\omega}_p = \omega_p / \eta_f$, based on conservation of fluid fluxes between the single and double porosity models.

In this study, when single continuum (single porosity model) is changed to dual continua (the double porosity model), the volume fractions of the secondary fracture and the rock matrix media are 0.1 and 0.9, respectively. The volume fraction of the fracture satisfies the constraint in Eq. (31) for the test cases. The solution procedure per unit time step is summarized in Table 2.

Table 2. The algorithm of the dynamic double porosity (dual continuum) model.

1.	Solve flow from the previously updated Lagrange's (reservoir) porosity and permeability.
2.	Obtain solutions of flow variables such as pressure, saturation, temperature.
3.	If a gridblock already has dual continua, upscale flow variables based on the formulation of double porosity model (Eq. 27 and Eq. 29).
4.	Solve geomechanics, taking the return mapping at the gridblock level.
5.	If there is a gridblock that faces failure, which consists of a single continuum, change it to the dual continuum model, updating the connectivity of subelements and gridblocks, if necessary.
6.	Update the permeability at the subelements of a gridblock that faces failure.
7.	Update Lagrange's porosity, drained bulk modulus, total strain at the subelement(s) of a gridblock (Eqs. 28-33).

8. Take the next time step.

Fig. 16(a) shows the enhanced permeability area at 29.4day for Case 1, when we employ the dynamic double porosity (dual continuum) model. Compared with the static single porosity (continuum) model (Fig. 4), the dynamic double porosity model yields faster failure, followed by the larger enhanced permeability areas, mainly because the permeability at the secondary fractures is higher than that of the single porosity model. Due to the fast failure, we obtain a higher rate of gas production than that of the reference case, shown in Fig, 16(b). Figs. 16(c) and 16(d) show evolution of pressure and permeability at P1 and P2, respectively. P1 faces failure at early times, having the increased permeability, earlier than P2. After both P1 and P2 faced failure, the pressures of P1 and P2 behave almost identically, because the two points are connected with high permeability. We also observe sudden pressure buildup at P1 when the area including P2 faces failure. This results from the flux increase induced by the enhanced permeability.

For Case 2, we find similar results to Case 1. We find significant failure areas that occur at early times, compared with the static single porosity model, as shown in Fig. 17(a). Faster failure inside the reservoir also enhances productivity because of high permeability (Fig. 17 (b)). In Figs. 17(c) and 17(d), we identify the increase of permeability at P5 and P6 induced by failure, followed by the non-smooth pressure evolution at P5 and P6 around 20day, at the time when failure occurs.

It should be noted that the proposed dynamic double porosity model is not always better than the single porosity model. The double porosity approach is fundamentally an approximation of the fine-scale single porosity model. In addition, we assume the volume fraction of the fracture medium to be given, not determined from the solution. When the stimulated volume of a failed gridblock is large, the failed gridblock can still be represented as a single continuum and the single porosity model can be used.

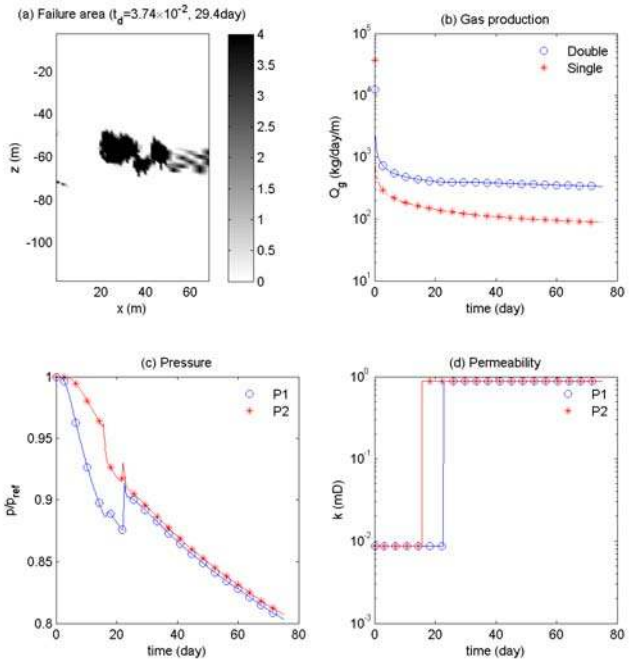

Fig. 16 (a) The failure areas of enhanced permeability for Case 1 at 29.4 day, (b) comparison of productivity between the static single continuum model and the dynamic double continuum model, (c) evolution of pressure at P1 and P2, and (d) evolution of permeability at P1 and P2. We obtain large failure at early times, followed by the increase of productivity, compared with the single continuum model, mainly because of the higher permeability at the fracture medium.

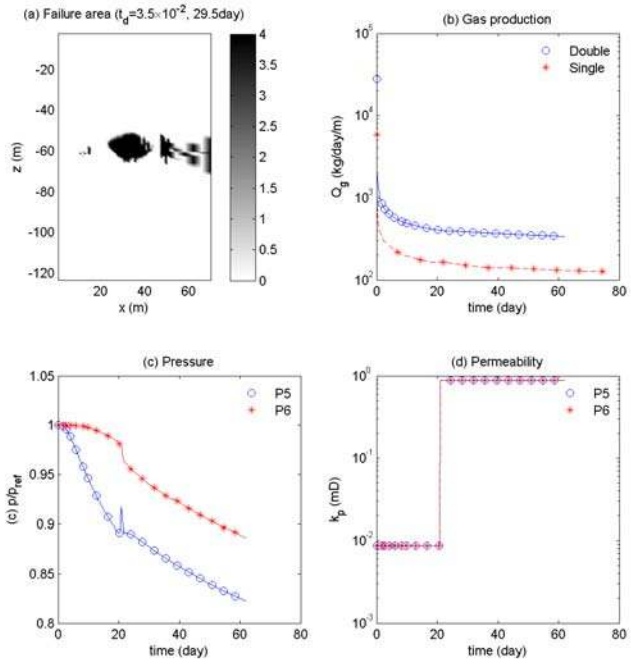

Fig. 17 (a) The failure areas of enhanced permeability for Case 2 at 29.5day, (b) comparison of productivity between the static single continuum model and the dynamic double continuum model, (c) evolution of pressure at P5 and P6, and (d) evolution of permeability at P5 and P6. The physical behaviors are similar to those of Case 1.

Summary and Conclusions

We investigated coupled flow and geomechanics in gas production from the extremely low permeability reservoirs such as tight and shale gas reservoirs, accounting for dynamic changes in pore volume and permeability. In particular, during simulation, permeability is updated every time step, which is based on the status of material failure.

We performed numerical tests for two cases: the horizontal and vertical primary fractures, considering the static single and dynamic double porosity models. The Mohr-Coulomb model was employed for modeling shear failure. For the single porosity model, we found that pressure drop at the production well caused failure not only near the fracture tips but also away from the well, increasing shear stresses significantly. Changes in permeability from material failure were significant, altering flow regimes dynamically. The changes in flow in turn affected geomechanics, causing further failure, followed by the propagation of the enhanced permeability areas. From various numerical tests, a large pressure drop at the production well induced more shear failure. High Biot's coefficient, low angles of friction and dilation, and smaller spacing between the horizontal wells also contributed to faster secondary fracturing. We introduced the dynamic double porosity model for secondary fracturing. From numerical simulation, we obtained different results from the single porosity model, because the fracture permeability of the double porosity model is higher than the permeability of the single porosity model. The different areas of the enhanced permeability were found, and the faster propagation of the areas was also observed. It is worth nothing that the fractures shown in this paper propagated stably for long time, and can be controlled by the bottom hole pressure and/or production time.

In conclusion, the physics in highly stress-sensitive or geomechanically weak reservoirs may not be captured accurately by flow only simulation or uncoupled simulation, and thus tightly coupled flow and geomechanics to model porosity and permeability are strongly recommended to predict potential secondary fracturing accurately. Then, we can design the production wells and/or production scenarios smartly, reducing cost of re-hydraulic fracturing and increasing productivity.

Acknowledgement

This study was supported by the US Environmental Protection Agency, Office of Water, under an Interagency Agreement with the U.S. Department of Energy at the Lawrence Berkeley National Laboratory through Contract No. DE-AC02-05CH11231, and by RPSEA (Contract No. 08122-45) through the Ultra-Deepwater and Unconventional Natural Gas and Other Petroleum Resources Research and Development Program as authorized by the US Energy Policy Act (EPAct) of 2005. The research described in this article has been funded by the U.S. Environmental Protection Agency through Interagency Agreement (DW-89-92235901-C) to the Lawrence Berkeley National Laboratory. The views expressed in this article are those of the author(s) and do not necessarily reflect the views or policies of the EPA.

Nomenclature

C : Volumetric heat capacity

$C_{p,f}$: Specific heat capacity of fluid

C_d : Total volumetric heat capacity

$\mathbf{C}_e$: Drained isothermal elasticity tensor

$\mathbf{C}_{up}$: Upscaled tangent moduli at the level of the gridblock

C_R : Heat capacity of the porous medium

$\mathbf{D}_J^k$: Hydrodynamic dispersion tensor

I_1, J_2, J_3 : Invariants of the effective stresses

$\mathbf{K}_H$: Composite thermal conductivity tensor of the porous media

K_{dr} : Drained bulk modulus

K_s : Intrinsic solid grain bulk modulus

K_l : Drained bulk modulus of material *l*.

$L_{l,m}(\equiv \mathbf{L})$: Biot's modulus matrix of the double porosity model

M : Biot's modulus

S_J : Saturation

$\overline{S}$, $\overline{s}$: Total entropy and specific entropy

T, T_0 : Temperature and reference temperature

X_J^k : Mass fraction of component *k* in phase *J*

c_f : Fluid compressibility

c_h : Cohesion

c_p : Pore compressibility

c_v : consolidation coefficient

e_J, h_J : Specific internal energy and enthalpy of components *k* in phase *J*

f, g : Yield and plastic potential functions

$\mathbf{f}_J^k$: Diffusive mass flows of component *k* in phase *J*

$\mathbf{g}$: Gravity vector

k: Absolute (intrinsic) permeability tensor.

k_K : Klinkenberg factor.

k_{rJ} : Relative permeability of phase *J*

k_0 : Intrinsic permeability

k_m : Intact rock permeability

m^k, $\mathbf{f}^k$, q^k : Mass, flux, source terms of component k.

$\mathbf{n}$: Normal vector of the boundary.

p_J, p_b : Pressure of phase *J,* bottom hole pressure, respectively

t: time

$\mathbf{u}$: Displacement vector

$\mathbf{w}_J^k$: Convective mass flows of component k in phase J

$\Delta x, \Delta z$: Horizontal and vertical grid spacing

Φ : Lagrange's (reservoir) porosity

$\Delta\Phi$: Porosity correction term

Ψ_f, Ψ_d, θ : Friction, dilation, and Lode's angles

Ω , Γ : domain , boundary

η_l : Volume fraction of material l.

α : Biot's coefficient

$\alpha_{m,\phi}$, $\alpha_{m,f}$: Coefficients of thermal dilation related to porosity and fluid

α_T : Thermal dilation coefficient

$\boldsymbol{\varepsilon}$: Total strain tensor

μ_J : Viscosity of phase J

ρ_J :, Density of phase J

ρ_R , Density of the porous medium,

ρ_b : Bulk density

$\boldsymbol{\sigma}$: Total stress tensor

$\boldsymbol{\sigma}'$: Effective stress tensor

σ'_m , τ'_m : Normal and shear effective stresses.

$\sigma_1', \sigma_2', \sigma_3'$: Maximum, intermediate, and minimum principal effective stresses

σ_v : Total volumetric mean stress.

$\bar{\sigma}$: geomechanical loading or overburden

τ_G : Gas tortuosity

ϕ : True porosity

ω_p : Permeability (or transmissibility) multiplier

$\tilde{\omega}_p$: Permeability (or transmissibility) multiplier for the fracture in the double porosity system

$\delta(\cdot)$: Variation relative to the motion of the solid skeleton.

$d(\cdot)/dt$: time derivative of a physical quantity $(\cdot)$ relative to the motion of the solid skeleton.

1: the second order identity tensor

Div, **Grad**: Divergence and gradient operators

tr $(\cdot)$: Trace of a second order tensor

References

Armero F. 1999. Formulation and finite element implementation of a multiplicative model of coupled poro-plasticity at finite strains under fully saturated conditions. *Comput. Methods Appl. Mech. Engrg.*171:205–241.

Armero F. and Simo J.C. 1992. A new unconditionally stable fractional step method for non-linear coupled thermomechanical problems. *Int. J. Numer. Meth. Engrg.* **35**: 737–766.

Armero F. and Simo J.C. 1993. A prior stability estimates and unconditionally stable product formula algorithms for nonlinear coupled thermoplasticity. *Int. J. Plasticity* **9**: 749–782.

Arthur J.D., Bohm B. and Layne M. 2008 Hydraulic fracturing considerations for natural gas wells of the Marcellus shale. Presented at the Ground Water Protection Council 2008 Annual Forum, Cincinnati, Ohio, USA, 21-24, Sep.

Aziz K. and Settari A. 1979. *Petroleum Reservoir Simulation*. London: Elsevier.

Bagheri M. and Settari A. 2008. Modeling of geomechanics in naturally fractured reservoirs. *SPE Reserv. Eval. Eng.* 11(1): 108–118.

Bai M. 1999. On equivalence of dual-porosity poroelastic parameters. *J. Geophys. Res.* **104**:10,461 – 10,466.

Barenblatt GE, Zheltov IP, Kochina IN. 1960 Basic concepts in the theory of seepage of homogeneous liquids in fissured rocks. *J. Appl. Math.*; 24(5):1286 – 1303.

Berryman JG. 2002 Extension of poroelastic analysis to double-porosity materials: New technique in microgeomechanics. *J. Eng. Mech.* ASCE; 128(8):840 – 847.

Borja R.I., Sama K.M., and Sanz P.F 2003. On the numerical integration of three-invariant elastoplastic constitutive models. *Comput. Methods Appl. Mech. Engrg.* **192**:1227–1258.

Cipolla C.L, Lolon E.P. and Erdle J.C. and Rubin. B. 2010 Reservoir modeling in shale-gas reservoirs. *SPE Reserv. Eval. Eng.* 638–653.

Coussy O. 1995. *Mechanics of porous continua*. Chichester, England: John Wiley and Sons.

Dean, R.H. and Schmidt, J.H., 2008 Hydraulic fracture predictions with a fully coupled geomechanical reservoir simulation SPE Annual Technical Conference and Exhibition, Denver, Colorado, 21 – 24 Sep.2008

Dusseault M.B., Bruno M.S., and Barrera J. 2001. Casing shear: Causes, cases, cures. *SPE Drilling & Completion* 16(2): 98–107. SPE-72060-PA

Eseme, E., Urai, J.L., Krooss, B. M., and Littke, R., 2007 Review of mechanical properties of oil shales: Implications for exploitation and basin modeling. *Oil Shale* **24**(2):159-174

Freeman C.M., Moridis G.J., and Blasingame T.A. 2011 A numerical study of microscale flow behavior in tight gas and shale gas reservoir systems. *Transp. Porous. Med.* 90:253–268

Fisher K. and Warpinski N. 2012 Hydraulic fracture-height growth: real data. *SPE Prod. Oper.* **27**(1):8-19

Gutierrez M.S. and Lewis R.W. 2002. Coupling of fluid and deformation in underground formations. *Eng Mech-ASCE* **128**(7): 779–787.

Hughes T.J.R. 2000. *The Finite Element Method: Linear Static and Dynamic Finite Element Analysis*. Englewood Cliffs, NJ: Prentice-Hall.

Hill, D.G. and Nelson, C.R.2000. Gas productive fractured shales: an overview and update. *Gas TIPS* **6**(3), 4–13.

Jenkins C.D. and Boyer C.M. 2008. Coalbed- and shale-gas reservoirs. *JPT* 92-99

Jha B. and Juanes R. 2007. A locally conservative finite element framework for the simulation of coupled flow and reservoir geomechanics. *Acta Geotechnica* **2**: 139–153.

Ji, L., and Settari A., and Sullivan, R.B. 2009. A novel hydraulic fracturing model fully coupled with geomechanics and reservoir simulation. *SPEJ*..423-430.

Kim J., Tchelepi H.A., and Juanes R. 2011a. Stability and convergence of sequential methods for coupled flow and geomechanics: Fixed-stress and fixed-strain splits. *Comput. Methods Appl. Mech. Engrg.* 200: 1591–1606

Kim J., Tchelepi H.A., and Juanes R. 2011b. Stability, Accuracy, and Efficiency of Sequential Methods for Coupled Flow and Geomechanics. *Soc. Pet. Eng. J.* **16**(2): 249–262. doi:10.2118/119084-PA.

Kim J, and Moridis G.J. 2013 Development of the T+M coupled flow-geomechanical simulator to describe fracture propagation and coupled flow-thermal-geomechanical processes in tight/shale gas systems. *Computers & Geosciences* In press.

Kim J. and Moridis G.J. and Yang D. and Rutqvist J.2012a Numerical studies on two-way coupled fluid flow and geomechanics in hydrate deposits. *SPEJ*.. **17**(2): 485–501. doi:10.2118/141304-PA

Kim J., Sonnenthal E., and Rutqvist J. 2012b Formulation and sequential numerical algorithms of coupled fluid/heat flow and geomechanics for multiple porosity materials. *Int. J. Numer. Meth. Engrg.* **92**:425-456, doi: 10.1002/nme.4340.

Lewis R.W. and Sukirman Y. 1993a. Finite element modelling for simulating the surface subsidence above a compacting hydrocarbon reservoir. *Int. J. Numer. Anal. Methods Geomech.* **18**: 619–639.

Lewis R.W. and Sukirman Y. 1993b. Finite element modelling of three-phase flow in deforming saturated oil reservoirs. *Int. J. Numer. Anal. Methods Geomech.* **17**: 577–598.

Lewis R.W., Makurat A., and Pao W.K.S. 2003. Fully coupled modelling of seabed subsidence and reservoir compaction of North Sea oil fields. *Hydrogeol J* **11**(1): 142–161.

Lewis R.W. and Schrefler B.A. 1998. *The finite element method in the static and dynamic deformation and consolidation of porous media*. Chichester, England: Wiley, 2nd edition.

McNamee J. and Gibson R.E. 1960a Displacement functions and linear transformations applied to diffusion through porous elastic media. *Q.J. Mech. Appl. Math.* **13**:98-111

McNamee J. and Gibson R.E. 1960b Plane strain and axially symmetric problems of the consolidation of a semi-infinite clay stratum. *Q. J. Mech. Appl. Math.* **13**:210-227

Nassir M., Settari A., and Wan R. 2012 Prediction and optimization of fracturing in tight gas and shale using a coupled geomechancial model of combined tensile and shear fracturing. Hydr. Frac. Tech. Conf. The woodland, TX, 6 – 8 Feb.

Nguyen V.X., and Abousleiman Y. N, 2010 Poromechanics solutions to plain strain and axisymmetric Mandel-type problems in dual-porosity and dual-permeability medium. *Journal of Applied Mechanics* 77: 011002.1-011002.18

Pao W.K.S. and Lewis R.W. 2002. Three dimensional finite element simulation of three-phase flow in a deforming fissured reservoir. *Comput Methods Appl. Mech. Engrg.* **191**: 2631–2659.

Pao W.K.S., Lewis R.W., and Masters I. 2001. A fully coupled hydro-thermo-poro-mechanical model for black oil reservoir simulation. *Int. J. Numer. Anal. Methods Geomech.* **25**(12): 1229–1256.

Pruess K. and Narasimhan TN. 1985 A practical method for modeling fluid and heat flow in fractured porous media. *SPEJ*. **25**(1):14 – 26.

Pruess, K., C. Oldenburg, and G. Moridis, 1999 TOUGH2 User's Guide, Version 2.0, Report LBNL-43134, Lawrence Berkeley National Laboratory, Berkeley, Calif.

Rutqvist J. and Stephansson O. 2003 The role of hydromechanical coupling in fractured rock engineering. *Hydrogeology J*. 11:7–40.

Settari A. and Mourits F. 1998 A coupled reservoir and geomechanical simulation system. *SPEJ*. 3:219–226.

Sondergeld C.H. and Newsham K. and Comisky J. and Rice M. and Rai C. 2010 Petrophysical considerations in evaluating and producing shale gas resources. Unconventional Gas Conf.. Pittsburgh, PA

Sukirman Y. and Lewis R.W. 1993. A finite element solution of a fully coupled implicit formulation for reservoir simulation. *Int. J. Numer. Anal. Methods Geomech.* **17**(10): 677–698.

Vermylen J.P. and Zoback M.D. 2011 Hydraulic fracturing, microseismic magnitudes, and stress evolution in the Barnett Shale. USA. Hydr. Frac. Tech. Conf. The woodland, TX, 24 – 26 Jan.

Wang X., Wang L.B., and Xu L.M. 2004 Formulation of the return mapping algorithm for elastoplastic soil models. *Comput. Geotech.* **31**:315–338.

White A.J. and Borja R.I. 2008 Stabilized low-order finite elements for coupled solid-deformation/fluid diffusion and their application to fault zone transients. *Comput. Methods Appl. Mech. Engrg*. 197:43534366.

Zoback M.D. 2007 *Reservoir geomechanics.* Cambridge, Cambridge university press.